Acta Crystallographica Section A
Foundations of Crystallography
ISSN 0108-7673

Received 25 August 2011
Accepted 27 October 2011

New consistency tests for high-accuracy measurements of X-ray mass attenuation coefficients by the X-ray extended-range technique

C. T. Chantler,[a]* M. T. Islam,[a,b] N. A. Rae,[a] C. Q. Tran,[c] J. L. Glover[a,d] and Z. Barnea[a]

[a]School of Physics, University of Melbourne, Australia, [b]School of Chemistry, University of Melbourne, Australia, [c]Department of Physics, La Trobe University, Australia, and [d]NIST, Ionizing Radiation Division, Gaithersburg, USA. Correspondence e-mail: chantler@unimelb.edu.au

An extension of the X-ray extended-range technique is described for measuring X-ray mass attenuation coefficients by introducing absolute measurement of a number of foils – the multiple independent foil technique. Illustrating the technique with the results of measurements for gold in the 38–50 keV energy range, it is shown that its use enables selection of the most uniform and well defined of available foils, leading to more accurate measurements; it allows one to test the consistency of independently measured absolute values of the mass attenuation coefficient with those obtained by the thickness transfer method; and it tests the linearity of the response of the counter and counting chain throughout the range of X-ray intensities encountered in a given experiment. In light of the results for gold, the strategy to be ideally employed in measuring absolute X-ray mass attenuation coefficients, X-ray absorption fine structure and related quantities is discussed.

1. Introduction

Important advances have been made over the past decade both in theory and in synchrotron measurements of X-ray absorption, as well as in understanding X-ray absorption fine structure (XAFS) and X-ray absorption near-edge structure (XANES) of materials (Joly *et al.*, 1999; Rehr & Albers, 2000; Rehr & Ankudinov, 2001; D'Angelo & Pavel, 2001; Kas *et al.*, 2010; Delgado-Jaime *et al.*, 2010). X-ray absorption spectroscopy (XAS) experiments are now mostly dependent on synchrotron sources, providing unparalleled scope for new experimental techniques in material analysis and accurate measurement of XAFS (Lytle, 2007; Chantler, 2010). A complete quantitative treatment of XAS is still challenging owing to a range of experimental and analytical complications (Rehr & Ankudinov, 2001; Smale *et al.*, 2006; Glover & Chantler, 2007; Delgado-Jaime & Kennepohl, 2010). Experimental methods can address potential impediments and optimistically lead to a quantitative treatment of XAS.

In this effort, the X-ray extended-range technique (XERT) (Chantler, Tran, Paterson & Barnea, 2001; Chantler, Tran, Barnea *et al.*, 2001; de Jonge *et al.*, 2005, 2006, 2007; Tran *et al.*, 2005; Chantler, 2009) consists of a suite of experimental techniques and procedures for their interpretation, leading to the quantitative treatment of XAS by measuring the X-ray mass attenuation coefficients $[\mu/\rho]$ in, and outside, the XAFS and XANES regions on an absolute scale. These techniques include:

(i) the use of multiple foils of different thicknesses selected beyond the extended Nordfors criterion (Nordfors, 1960; Creagh & Hubbell, 1987);

(ii) measurement over a wide range of energies;

(iii) monitoring of the incident synchrotron X-ray beam by an (ion chamber) counter and comparison of the incident and attenuated beams by a matched (ion chamber) counter;

(iv) accurate determination of the energy of the X-ray beam at which the X-ray mass attenuation coefficient is measured;

(v) allowance for the energy resolution and bandpass of the incident-beam monochromator in the vicinity of absorption edges;

(vi) careful determination of the X-ray fluorescence and scattering background;

(vii) testing of the intensity range of the linear response of the counters;

(viii) determination of the fraction of higher-order harmonic energy photons present in the incident monochromated X-ray beam;

(ix) comparison of the relative thicknesses of the foils used in the measurements at the point at which the X-ray beam passes through the foil (sometimes referred to as the thickness transfer method, TTM);

(x) point-by-point raster measurements of the attenuation of a selected foil and determination of the corresponding column density at each measured point, leading to the absolute determination of the mass attenuation coefficient and

related quantities including atomic form factors and XAFS; and

(xi) the point-by-point raster scans are matched to careful measurement of the mass and area of test samples, thereby giving their mean thickness or integrated column density.

As can be seen from items (ix) and (x) above, so far our method involved comparing the thicknesses of the samples used by an attenuation measurement relative to a single reference sample whose thickness and absolute mass attenuation were obtained from an X-ray raster scan combined with a determination of the mass m and area A of the reference sample (TTM).

Now we propose, in addition, to use raster scans for independent determinations of the absolute thicknesses and mass attenuations of several samples of different thicknesses – the multiple independent foil technique (MIFT). This allows us to improve and test three further aspects of the consistency of our measurements:

(a) the raster scans allow us to test the uniformity of the thickness of the samples and hence to select the most uniform amongst them and thus obtain more accurate mass attenuation coefficients;

(b) the independent absolute mass attenuation determinations can be compared with the thickness determinations relative to a single sample (the TTM);

(c) the linearity of the response of the X-ray detector and its counting chain can be tested in the exact range of X-ray intensities encountered in the course of the attenuation measurements.

To illustrate the value of the MIFT, we will describe the absolute mass attenuation coefficient measurement of gold foils, compare the MIFT results with the TTM, demonstrate the linearity of the response of the ion chambers as configured and discuss the strategy that results in the most accurate determination of the mass attenuation coefficients.

2. Overview

XERT enables critical comparison between experiment and theory (Tran, Chantler & Barnea, 2003). While the original idea is relatively straightforward (Chantler *et al.*, 1999), and developed earlier ideas of Barnea, Creagh and others (Mica *et al.*, 1985), the detailed implementation has yielded an extraordinary richness of physical insight and technical development, giving rise recently to two new fields: of nanoroughness measurement (Glover *et al.*, 2009) and inelastic mean-free-path measurement (Bourke & Chantler, 2010; Chantler & Bourke, 2010).

The accuracy of measured X-ray mass attenuation coefficients depends strongly on how the thickness or integrated column density $[\rho t]_c$ of the absorbing specimen has been measured (Tran, Chantler *et al.*, 2004; Tran *et al.*, 2005). Measurement techniques for investigating sample thickness or $[\rho t]_c$ are, therefore, a crucial experimental issue for the accuracy of the measured quantities (Rae, Islam *et al.*, 2010). The XERT has been used for high-accuracy measurements of X-ray mass attenuation coefficients, form factors, absorption fine structure (de Jonge *et al.*, 2005) and bond length (Glover *et al.*, 2010) by using multiple foils, and thereby allowing the detection and correction of a number of systematic errors including harmonics (Tran, Barnea *et al.*, 2003; Glover & Chantler, 2009), scattering and fluorescence (Tran, de Jonge *et al.*, 2004), finite-spectral bandwidth (de Jonge *et al.*, 2004*a*), sample roughness (Glover *et al.*, 2009) and air attenuation.

A variety of methods have been used to determine sample thicknesses or integrated column densities $[\rho t]_c$ for the determination of attenuation. Previous measurements of X-ray mass attenuation coefficients used average sample thicknesses t_{av} (Gerward, 1983, 1989; Wang *et al.*, 1992, 1994). Many recent measurements of X-ray mass attenuation coefficients have used local thicknesses (Tran, Chantler *et al.*, 2004; Tran *et al.*, 2005) or integrated column densities $[\rho t]_c$ (de Jonge *et al.*, 2004*b*; Islam *et al.*, 2010; Rae, Chantler *et al.*, 2010). In these latter measurements, the local thickness t_c or the integrated column density $[\rho t]_c$ of a reference foil is measured on an absolute scale, at the point through which the direct beam passes during the measurement, and then t_c or $[\rho t]_c$ of other foils are determined to high accuracy by comparison with the reference foil following the TTM. We weigh the foil with an accurate mass balance, repeatedly; we profile the area of the foil using a microscope with an accurate stage; we therefore have a rigorous accuracy on the average mass per unit area; we check coarse structure with a micrometre; and we X-ray profile the foil to generate a detailed map of the structure and thickness (of integrated column density) in the beam.

Here we present a new approach – the multiple independent foil technique (MIFT) – for the measurement of $[\rho t]_c$, and apply this to attenuation measurements of four gold foils using XERT. We thereby measure X-ray mass attenuation coefficients four times on an absolute scale independently, and investigate the robustness and the consistency of the error analysis. The measured X-ray mass attenuation coefficients are compared with results (Islam *et al.*, 2010) obtained by the TTM and are found to be in excellent agreement.

The MIFT approach can characterize a preferred set of reference standards for high-accuracy investigation. A not-uncommon occurrence to date includes apparent discrepancies, *e.g.* for X-ray attenuation for standard material of order 10% (Glover *et al.*, 2010; Laubert, 1941; Rao, 1978; Rae, Chantler *et al.*, 2010; Hopkins, 1959; Unonius & Suortti, 1989; de Jonge *et al.*, 2007). Similarly, quoted standards (*e.g.* iron foils of different thickness, roughness, flatness and oxidation) may be unstable and apparently beamline or source dependent.

Our new approach achieves accuracies down to 0.15% in this study, though improvements will certainly result in even lower uncertainties – the new approach may be used to investigate the accuracy of earlier methods down to this level. Importantly, the measurements provide stringent tests of the linearity of the detector chain across several decades, permitting questions of the optimization or limitations of particular detector systems to be directly investigated, either for further improvements in XAFS or for more generalized experimental methods.

3. Experiment

The experimental configuration is shown in Fig. 1. A bending magnet was used to produce an X-ray beam at the 1-BM XOR beamline of the Advanced Photon Source (APS) synchrotron at the Argonne National Laboratory.

To select the X-ray beam energy, the beam was monochromated by reflection from the (400) planes of a pair of silicon crystals located in the first optical enclosure. The monochromated X-rays were then passed through a pair of adjustable slits to define the beam cross section of approximately 2×2 mm. To determine the beam energy, a sodium iodide scintillation counter, located on the detector arm of a six-circle Huber diffractometer, was used to record the angular location of a number of reflections from the standard powder Si640b (Parrish *et al.*, 1999). For the beam intensity to be monitored and measured, ion chambers were located upstream and downstream from the attenuating foils.

Four gold foils with nominal thicknesses between 9.3 and 275 µm were used for the attenuation measurements. Each foil was raster-scanned using an X-ray beam over the central 8×8 mm area to determine its X-ray attenuation profile. X-ray attenuation profiles of the central areas of the foils are shown in Fig. 2. Conventional measurement of X-ray mass attenuation coefficients required satisfaction of the Nordfors criterion for sample thickness (Creagh & Hubbell, 1987, 1990) on the basis of statistical quality. However, we have demonstrated that higher accuracy results from multiple thicknesses sampled over a much wider range of attenuation ratios.

4. Analysis

We analyzed the data set containing upstream and downstream repeated measurements with different apertures for each sample. The attenuation by each region of a given foil was determined using

$$[\mu t] = \left[\frac{\mu}{\rho}\right][\rho t] = \ln \frac{[(I - D)/(I_0 - D_0)]_s}{[(I - D)/(I_0 - D_0)]_b}, \qquad (1)$$

where I is the attenuated intensity, I_0 is the unattenuated intensity and D is the recorded dark current. The subscripts s and b represent the measurements with a sample in the path of the X-ray beam and without a sample in the path, respectively. Attenuation profile measurements were made at 25 points across the central 8×8 mm area of each of the foils using equation (1). This allows for measurement and correction for electronic noise, air path and detector efficiency (Chantler, 2009).

The integrated column density $[\rho t]_c$ of each foil at the central point c where the beam passed through the foil was obtained from the average attenuation $[\mu t]_{av}$ obtained from the raster scan, from the attenuation $[\mu t]_c$ at the point c, and the average integrated column density $[\rho t]_{av} = m/A$, where m is the mass and A is the area of the foil. $[\rho t]_c$ is then

$$[\rho t]_c = \frac{[\mu t]_c}{[\mu t]_{av}} \times [\rho t]_{av}. \qquad (2)$$

The corresponding uncertainties of $[\rho t]_c$, presented in Table 1, were determined combining the uncertainty contributions in $[\mu t]_c$, $[\mu t]_{av}$, m and A of the respective foil as

$$\left[\frac{\sigma_{[\rho t]_c}}{[\rho t]_c}\right] = \left(\left[\frac{\sigma_{[\mu t]_c}}{[\mu t]_c}\right]^2 + \left[\frac{\sigma_{[\mu t]_{av}}}{[\mu t]_{av}}\right]^2 + \left[\frac{\sigma_m}{m}\right]^2 + \left[\frac{\sigma_A}{A}\right]^2\right)^{1/2}. \qquad (3)$$

As seen in Table 1, the uncertainty in $[\rho t]_c$ obtained using MIFT is smallest for the thickest 275 µm foil whose attenuation was best determined and which displayed the smallest variation in the raster scan (Fig. 2). The fractional uncertainty increases with decreasing foil thickness as the variation across the foil increases, and is, as one would expect, greatest for the

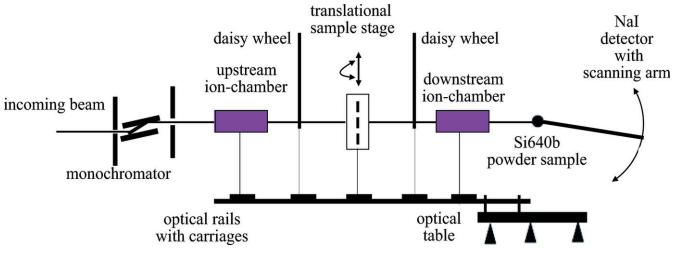

Figure 1
Experimental setup of the XERT at the APS on which data were collected for this analysis. Ion chambers are located upstream and downstream from the attenuating samples to monitor and measure the beam intensity. The daisy wheels carry attenuation foils and apertures of various sizes for determining the harmonic contamination of the X-ray beam and the X-ray scattering and fluorescence contributions (Tran, de Jonge *et al.*, 2004).

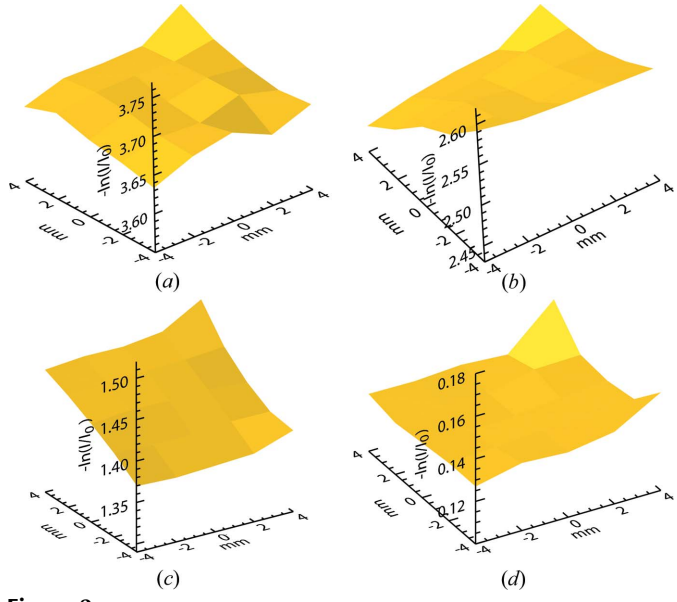

Figure 2
The X-ray attenuation profiles of the central regions of four gold foils, resulting from the raster scans. (*a*) corresponds to the nominally 275 µm-thick foil at 50 keV. (*b*) corresponds to the nominally 116.5 µm-thick foil at 42 keV. (*c*) and (*d*) correspond to 100.6 and 9.3 µm-thick foils, respectively, both measured at 50 keV. The variations of foil attenuation on the X-ray maps were found to be in the ranges of (−0.64% → +0.74%), (−2.61% → +2.52%), (−4.47% → +3.05%) and (−3.6% → +12%) for the nominally 275, 116.5, 100.6 and 9.3 µm-thick foils, respectively.

Table 1
Measured $[\rho t]_c$ of four gold foils using the MIFT and TTM.

The first column lists the nominal thicknesses of the gold foils. The second column lists $[\rho t]_c$ of the foils determined with the MIFT and the third column lists $[\rho t]_c$ values using the TTM. Measurements were made as indicated in the text and in Fig. 2. The MIFT values are measured using independent X-ray area scans of the foils.

	$[\rho t]_c$ (g cm^{-2})	
t_{nom} (μm)	MIFT	TTM
275.0	0.5124 ± 0.053%	0.5115 ± 0.10%
116.5	0.2244 ± 0.279%	0.2240 ± 0.11%
100.6	0.1943 ± 0.398%	0.1972 ± 0.12%
9.3	0.0174 ± 0.883%	0.0177 ± 0.17%

thinnest and least uniform 9.3 μm foil with relatively weak attenuation.

In view of these results, it is natural to choose the 275 μm foil as the reference foil relative to which the thicknesses of the other foils should be determined if using the thickness transfer method. This use of the MIFT to test the quality of reference samples is one of its most important benefits.

The uncertainties in $[\rho t]_c$ of the foils were found to be relatively larger using MIFT compared to TTM (Table 1). This is due to the fact that in the TTM, the non-uniformity of the secondary foils is irrelevant, and only the non-uniformity of the reference foil contributes to the error; whereas in the MIFT, each foil contributes an uncertainty due to its own non-uniformity. The 116 and 9.3 μm-thick foils are non-uniform and approximate wedges (see Fig. 2), so the uncertainties of these foils are increased and contribute larger uncertainties to the final results.

Uncertainty contributions in $[\rho t]_c$ of each foil can be treated independently using MIFT. This approach thus allows the detection of the error sources of measured $[\mu/\rho]$ related to any specific foil due to local structure or poor quality of sample or of data collected. Where several thicknesses of foil of good quality are available, the MIFT will also yield superior results.

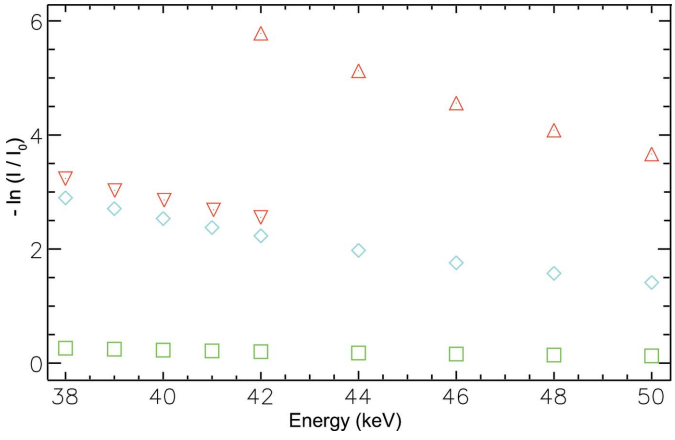

Figure 3
The foil attenuations of four gold foils with different thicknesses in the 38–50 keV energy range. The symbols □ represent the attenuation by the foil with nominal thickness 9.3 μm, ◇ a nominal thickness of 100.6 μm, △ a nominal thickness of 275 μm and ▽ a nominal thickness of 116.5 μm.

5. X-ray mass attenuation of gold

Fig. 3 presents the total mass attenuation measured using four gold foils with different thicknesses, as a function of energy (Islam *et al.*, 2010). X-ray mass attenuation coefficients are determined by dividing the foil attenuations $[\mu/\rho][\rho t]$ by the $[\rho t]_c$ for the given foil. The final value of $[\mu/\rho]$ at a given energy was then obtained from the weighted mean of $[\mu/\rho]_i$ measured with different foil thicknesses using

$$[\mu/\rho] = \sum_i \frac{[\mu/\rho]_i}{\left[\sigma_{[\mu/\rho]}\right]_i^2} \Bigg/ \sum_i \frac{1}{\left[\sigma_{[\mu/\rho]}\right]_i^2}, \qquad (4)$$

where $[\mu/\rho]_i$ are the measured mass attenuation coefficients derived from different thicknesses and $\sigma_{[\mu/\rho]_i}$ are the corresponding uncertainties (standard errors).

The uncertainty in $[\mu/\rho]$ was determined from the uncertainty contribution from $[\rho t]_c$ and the standard deviation of counting statistics of the repeated measurements. The final uncertainty was determined from the weighted mean of $\sigma_{[\mu/\rho]_i}$ as

$$\sigma_{[\mu/\rho]} = \left\{ \frac{\sum_i \left(\left([\mu/\rho]_i - \overline{[\mu/\rho]} \right) / \sigma_{[\mu/\rho]_i} \right)^2}{(N-1) \sum_i 1/\sigma^2_{[\mu/\rho]_i}} \right\}^{1/2}. \qquad (5)$$

6. Investigation of linearity of detector chain

Fig. 4 illustrates the attenuation log ratios for all reference samples measured at two energies. The second crystal of the monochromator is detuned to eliminate harmonics, which is effective down to approximately 7 keV X-ray energies. Harmonics are explicitly measured down to approximately one part in 10^4 by our experimental technique including daisy wheels (Tran, Barnea *et al.*, 2003; Rae, Chantler *et al.*, 2010). Since at higher energies harmonics are generally negligible (Barnea *et al.*, 2011), the plots measure the linearity of the detector and counting chain. That is, they measure the treatment of dark current, air path and scattering – which are non-linear processes – but especially the detector response function, which is highly non-linear near saturation, when flux density is high and recombination in the gas detector is significant, or when artefacts including amplifier non-linearities are significant. The plots show that, over three decades of attenuation, this whole response chain is linear so that highly accurate results can be obtained.

Scattering is not a topic of this paper, but small apertures (as we use to measure the effects) or larger ion-chamber windows still measure significant forward scattering and fluorescence (for the downstream detector), and backward scattering and fluorescence (for the upstream monitor) which commonly is in the 0.01–6% range (a function of energy and geometry), and is clearly non-linear (Tran, de Jonge *et al.*, 2004; Chantler, Tran, Paterson, Barnea & Cookson, 2001; Rae, Chantler *et al.*, 2010). Often fluorescence will dominate above the absorption edge, especially because of its *prima facie* isotropic dependence. We directly measure this so it can be

subtracted and does not affect the measurement. Because our solid angles are small by design, the effect and correction are small.

The plots prove that electron–ion recombination is not an issue at the current incident X-ray flux (specifically the flux density) at the ion chamber; the current gas mixture, density and absorption coefficient; and for the explicit ion-chamber geometry and electric-field strength. Occasions where this does occur for ion chambers and other detectors are not uncommon at synchrotrons and can be estimated broadly from the literature (Chantler & Staudenmann, 1995). Methods for correcting or estimating recombination losses include the often-used quadratic term in flux density, effective near to saturation and explicitly non-linear in lowest order (Takata *et al.*, 1999; Pettifer *et al.*, 1999; Park *et al.*, 2005). More detailed discussions from different perspectives are given elsewhere (Chantler & Staudenmann, 1995; Kirsanov & Obodskiy, 2010). Whenever recombination non-linearities occur the quadratic term at least is explicitly obvious.

The similar effect of saturation of the detection electronics depends upon the amplifier, shaping time and explicitly dead time of the counting chain, including the ion chamber. This is also strongly non-linear when it occurs, but is not observed in our data at the level presented.

Many investigations use detectors (charge-coupled devices, pixel-based or imaging detectors) which may only be linear to a few percent or which may only be linear over a single decade (Barnea *et al.*, 2011). The type of investigation outlined here, which will allow determination of beamline-specific effects dependent on the geometry of the experiment and thereby permit determination of beamline-independent results for attenuation or XAS, is invaluable in assigning a confidence level to final results.

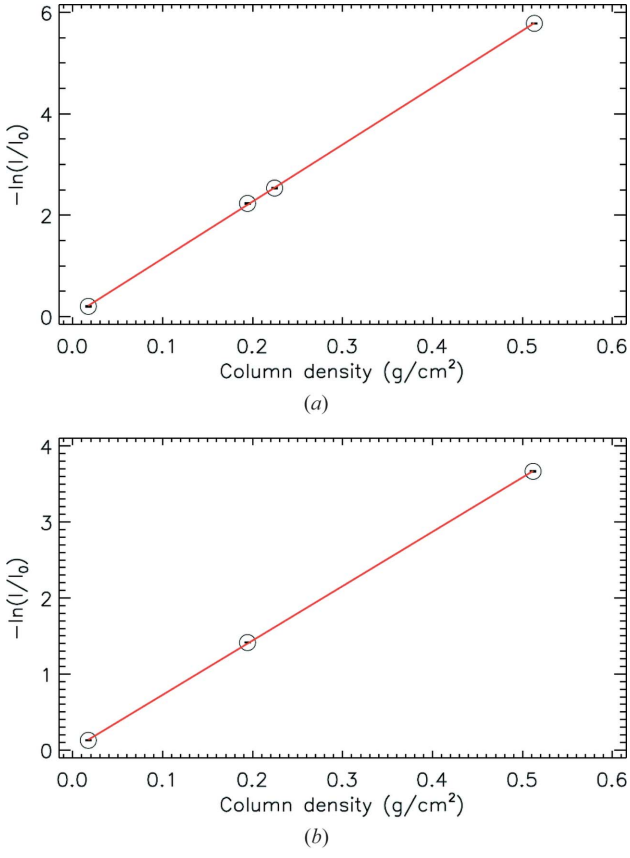

Figure 4
The independent measurements of foil thickness and integrated column density may be used to assess the detector and counting linearity at different energies, especially where large ranges of thickness are used. Plotted here are results for (*a*) 42 keV and (*b*) 50 keV, showing remarkable linearity and confirming that systematics and ion-chamber performance are optimized for this experiment.

7. Investigation of inconsistencies of independently measured samples – searching for high-quality reference samples

Fig. 5, by contrast, focuses on minor discrepancies between the results of the four different, independently measured samples. From the plot, it is obvious that the two thickest, independently measured samples are in excellent agreement, within one standard deviation of the weighted mean and with small uncertainty. The thinner two foils had relatively large uncertainty from the statistical determination, from the uncertainty of the mass and area, and from their wedge-like structure – as explained earlier – and so it is in fact no surprise that these samples are less consistent.

In the current situation, the two thinner, poorer samples are only two or three standard errors discrepant, so all are 'relatively good' within their quoted uncertainties. The consistency

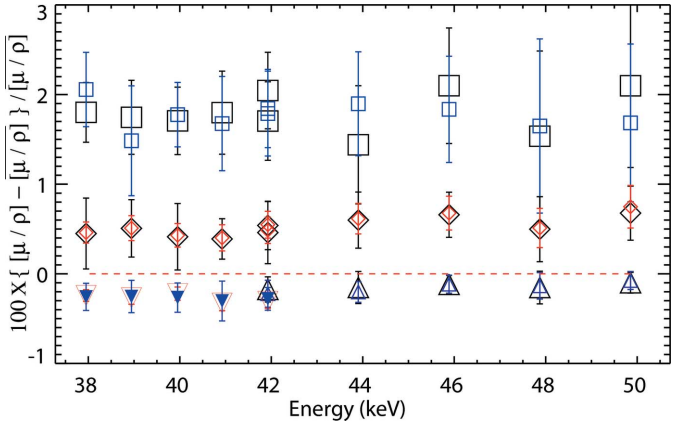

Figure 5
A comparison of the detailed agreement at all energies of the independent data for each independently measured sample. Each symbol represents a separate independent evaluation using a different aperture detector, *i.e.* the larger open squares represent data using a larger detector aperture, the smaller open squares represent data collected using a smaller detector aperture – clearly all of these are consistent. The weighted mean is dominated by results for the thickest (275 μm, △) foil, as expected. This is consistent within one standard error (s.e.) with the second thickest foil (116.5 μm, ▽) including at the transfer point of 42 keV. The two thinner foils (9.3 μm, □; 100.6 μm, ◇) were relatively poorly determined owing to statistics and uncertainty in m/A, and owing to their wedge-like structure. A small 2 s.e. systematic due to the wedges, particularly for the thinnest foil, indicates that these determinations are indeed less reliable. Inconsistency is dominated by the error in the absolute determination of the thickness of the □ 9.3 μm foil.

Table 2
Measured $[\mu/\rho]$ in the 38–50 keV energy range and the corresponding percentage standard deviation uncertainties.

The first column lists the measured energies (for energy calibration see Rae *et al.*, 2006; Rae, Islam *et al.*, 2010), the second column lists the $[\mu/\rho]$ with the MIFT and the third column lists $[\mu/\rho]$ with the TTM. The $[\mu/\rho]$ values listed in the fourth column (the optimized result) are determined from the weighted mean of $[\mu/\rho]$ measured with the MIFT and TTM approaches. Qualitatively larger uncertainties were observed in the measurements with the thinnest foil using the MIFT. Numbers in parentheses are the standard deviations of the parameter in the least significant digits.

	$[\mu/\rho]$ ($cm^2\ g^{-1}$) % s.d.					
E_{cal} (keV)	MIFT		TTM		Optimized result	
37.95137 (29)	14.7382 (426)	0.288%	14.6962 (32)	0.102%	14.7008 (141)	0.0962%
38.94325 (30)	13.7739 (374)	0.271%	13.7352 (17)	0.101%	13.7399 (130)	0.0947%
39.95217 (31)	12.8870 (351)	0.272%	12.8518 (13)	0.101%	12.8562 (122)	0.0947%
40.92519 (32)	12.0869 (332)	0.274%	12.0540 (18)	0.101%	12.0579 (114)	0.0948%
41.92506 (35)	11.3243 (305)	0.269%	11.3171 (30)	0.102%	11.3180 (108)	0.0954%
43.90285 (51)	10.0020 (163)	0.163%	10.0214 (15)	0.101%	10.0160 (86)	0.0858%
45.88667 (62)	8.9002 (134)	0.151%	8.9164 (16)	0.102%	8.9113 (75)	0.0844%
47.87059 (94)	7.9738 (121)	0.152%	7.9821 (19)	0.103%	7.9795 (68)	0.0853%
49.8545 (11)	7.1559 (112)	0.156%	7.1685 (10)	0.101%	7.1648 (61)	0.0849%

of results presented in this plot establishes the high level of confidence in both the detector linearity – which would otherwise lead to systematic deviations with energy and thickness – and in the individual independently measured samples.

All foils are held in carefully constructed plastic mounts on a stage accurate to 1 µm. Each foil is rotated by rotation stages to ensure perpendicularity with the beam. Any other orientational defects are addressed by either the TTM (which ensures that the local region of a secondary foil is exactly calibrated to that of the reference for which the alignment is determined) or by the MIFT, which confirms and checks each orientation.

8. Comparison of the TTM and of theory and experiment

The X-ray mass attenuation coefficients were also analyzed (Islam *et al.*, 2010) using the TTM. There, the $[\rho t]_c$ of a single reference foil was measured on an absolute scale and the relative values of $[\rho t]_c$ of other foils were determined relative to the reference foil. The $[\mu/\rho]$ obtained from the MIFT is compared with the $[\mu/\rho]$ obtained by the TTM in Table 2.

Fig. 6 shows a comparison of $[\mu/\rho]$ obtained by the MIFT and by the TTM. The solid line represents the weighted mean of the X-ray mass attenuation coefficients obtained by the two methods (see Table 2). In this plot, the X-ray mass attenuation coefficients $[\mu/\rho]$ obtained by both methods appear to be in very close agreement.

The percentage difference of the X-ray mass attenuation coefficients $[\mu/\rho]$ from the weighted mean, as shown in Fig. 7, reveals the consistency and accuracy of the measurements of $[\rho t]_c$ with the MIFT compared to TTM. The results with the MIFT deviated by from −0.3% to +0.2% compared with the results of the TTM. The measured $[\mu/\rho]$ (represented by □ in Fig. 7) using the $[\rho t]_c$ by the MIFT is consistent with those using TTM within their uncertainties.

The discontinuity in Fig. 7 is due to the necessary change of foil, as the thickest foil had too high an attenuation at lower energies. The 'cost' of this necessary transfer is represented by the uncertainties given. In this particular investigation, the thinnest foil provided relatively poor statistics and the two thinner foils were wedge shaped. The limitations of the shapes of these thinner foils provide a source of uncertainty for the MIFT and limit the value of the technique in this instance. However, if several uniform foils are available and determined to high accuracy, the MIFT can be significantly superior to the TTM approach.

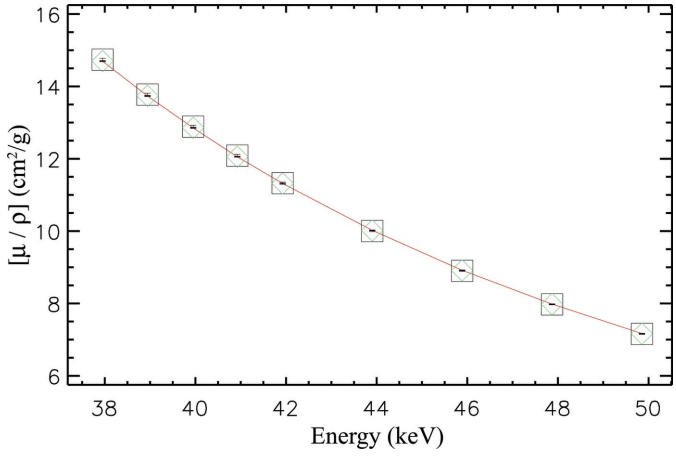

Figure 6
A comparison between $[\mu/\rho]$ measured with the values of $[\rho t]_c$ determined by MIFT and TTM methods. The results are in excellent agreement. The solid line represents the weighted mean values of $[\mu/\rho]$ with the two methods. The symbols □ represent the results using the MIFT, and the symbols ◇ give results from the thickness transfer method, TTM. The uncertainties are smaller than the size of the symbols.

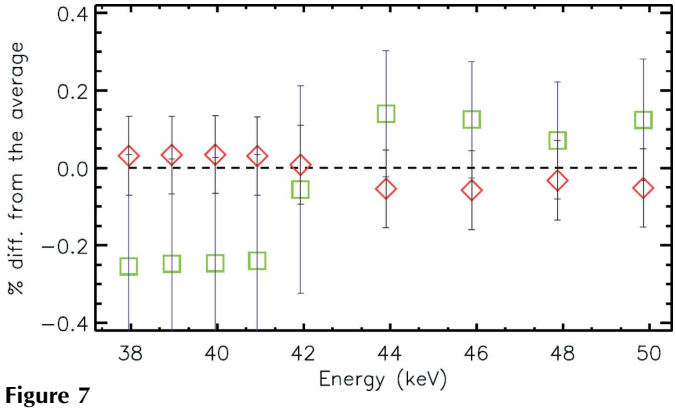

Figure 7
Percentage difference of $[\mu/\rho]$ from the weighted mean values of $[\mu/\rho]$ obtained by MIFT and TTM methods. ◇ represents the $[\mu/\rho]$ obtained by the TTM, and □ represents results using the MIFT. Results are consistent within their standard errors.

The data of two different theoretical tabulations, FFAST (Chantler, 2000) and XCOM (Saloman *et al.*, 1988), and experimental measurements are compared in Fig. 8. While the MIFT and TTM results are consistent within uncertainty, this figure points to large errors of previous experimental work, compared to theory; illustrates significant deviation from atomic theory and standard reference works; and confirms the likely accuracy of both presented theoretical predictions to approximately 1%.

This investigation could be used to isolate error sources related to any individual foil from its independent attenuation profile, and from the counting statistics with the foil itself, which is one of the key objectives of high-accuracy measurements. Previous XERT measurements could not consider the MIFT, owing to the availability of the experimental setup – but, where possible, this approach can significantly reduce the uncertainty in the final results.

9. Discussion and further work

X-ray mass attenuation coefficients of gold were measured in the 38–50 keV energy range employing two different methods of the XERT. The new MIFT technique was used successfully and the consistency between the measurements by the MIFT and TTM methods was tested. The results with the TTM rely on the 275 µm reference foil and the error sources with other foils are explained on a relative scale. In contrast, the results with the MIFT are independent from each other as there is no reference foil. The $[\rho t]_c$ values obtained by this method are independent of each other, so for example relatively poor standards can be identified by systematic variations in sample attenuation. Poor samples, perhaps due to non-ideal thickness or dramatic wedge structure, can be identified using the comparison between MIFT and TTM and corresponding raster scans, and corrected by either omitting such data or by using MIFT for high-quality samples and the TTM to transfer to the poorer samples without loss of data. This method thus provides an important option to identify and correct uncertainty contributions from the foil metrology to achieve highly accurate results.

In future XERT experiments, the full-foil mapping of all foils at each energy is recommended to test consistency between the measurements with different foils and different methods. Another interesting experiment could use full-foil mapping of all experimental foils to determine the $[\rho t]_c$ of the foils on an absolute scale and thereby measure absolute XAFS spectra with even greater accuracy. This investigation might also be a reliable test of the counting statistics of the response of the counting chain in the ion chambers. Careful application of this new method should reveal new physical processes (for example, significant new information on scattering and nanoroughness) and permit recognition and optimization of new systematic signatures (such as due to defective absolute calibrations, inappropriate choice of standards but also as-yet unexplored systematics at the 0.1% level and below). Specific advantages are:

(i) the measurements with each foil become independent;

(ii) for a given energy the mass absorption coefficients for each sample can be derived and compared for consistency or for uncertainties in sample preparation technique;

(iii) the linearity of the response of the counters is explicitly tested by the MIFT, across the range represented by the sample thicknesses, and is a powerful method to diagnose detector or amplifier non-linearity; and

(iv) a comparison of results using MIFT and TTM can be used to test the quality of the methods and the consistency of the experimental data.

The additional time and effort required to carry out independent multiple-sample measurements and X-ray profilometry is modest (a few hours or less), and the results have proved to be a sensitive test of measurement consistency and linearity.

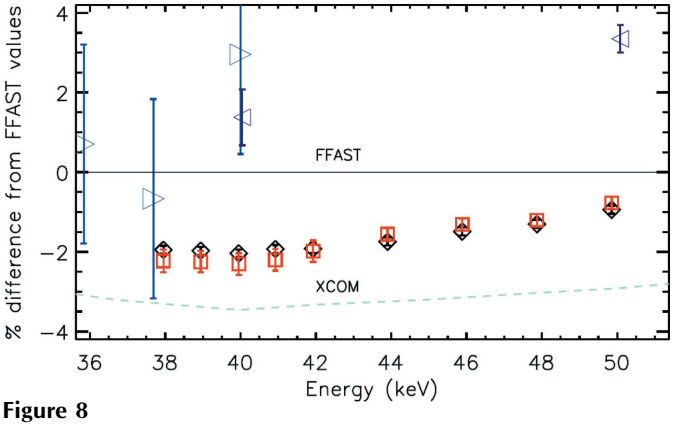

Figure 8
The measurements of $[\mu/\rho]$ of this work [◇ (TTM); □ MIFT] are compared with the theoretical predictions of FFAST and XCOM tabulations, and with other experimental results in this energy range. Two experimental measurements (McCrary *et al.*, 1967; Laubert, 1941) are represented by the symbols ◁ and ▷, respectively.

The work was funded by the Australian Research Council. The authors would like to thank the APS where the experiment was performed, and the Australian synchrotron access program.

References

Barnea, Z., Chantler, C. T., Glover, J. L., Grigg, M. W., Islam, M. T., de Jonge, M. D., Rae, N. A. & Tran, C. Q. (2011). *J. Appl. Cryst.* **44**, 281–286.
Bourke, J. D. & Chantler, C. T. (2010). *Phys. Rev. Lett.* **104**, 206601.
Chantler, C. T. (2000). *J. Phys. Chem. Ref. Data*, **29**, 597–1048.
Chantler, C. T. (2009). *Eur. Phys. J.* **169**, 147–153.
Chantler, C. T. (2010). *Radiat. Phys. Chem.* **79**, 117–123.
Chantler, C. T., Barnea, Z., Tran, C. Q., Tiller, J. & Paterson, D. (1999). *Opt. Quant. Elect.* **31**, 495–505.
Chantler, C. T. & Bourke, J. D. (2010). *J. Phys. Chem. Lett.* **1**, 2422–2427.
Chantler, C. T. & Staudenmann, J.-L. (1995). *Rev. Sci. Instrum.* **66**, 1651–1654.
Chantler, C. T., Tran, C. Q., Barnea, Z., Paterson, D., Cookson, D. J. & Balaic, D. X. (2001). *Phys. Rev. A*, **64**, 062506.
Chantler, C. T., Tran, C. Q., Paterson, D. & Barnea, Z. (2001). *Phys. Lett. A*, **286**, 338–346.

Chantler, C. T., Tran, C. Q., Paterson, D., Barnea, Z. & Cookson, D. J. (2001). *Radiat. Phys. Chem.* **61**, 250–347.
Creagh, D. C. & Hubbell, J. H. (1987). *Acta Cryst.* A**43**, 102–112.
Creagh, D. C. & Hubbell, J. H. (1990). *Acta Cryst.* A**46**, 402–408.
D'Angelo, P. & Pavel, N. V. (2001). *J. Synchrotron Rad.* **8**, 173–177.
Delgado-Jaime, M. U. & Kennepohl, P. (2010). *J. Synchrotron Rad.* **17**, 119–128.
Delgado-Jaime, M. U., Mewis, C. P. & Kennepohl, P. (2010). *J. Synchrotron Rad.* **17**, 132–137.
Gerward, L. (1983). *Acta Cryst.* A**39**, 322–325.
Gerward, L. (1989). *Acta Cryst.* A**45**, 1–3.
Glover, J. L. & Chantler, C. T. (2007). *Meas. Sci. Technol.* **18**, 2916–2920.
Glover, J. L. & Chantler, C. T. (2009). *X-ray Spectrom.* **38**, 510–512.
Glover, J. L., Chantler, C. T., Barnea, Z., Rae, N. A. & de Jonge, M. D. (2010). *J. Phys. B At. Mol. Opt. Phys.* **43**, 085001-1-15.
Glover, J. L., Chantler, C. T. & de Jonge, M. D. (2009). *Phys. Lett.* **373**, 1177–1180.
Hopkins, J. I. (1959). *J. Appl. Phys.* **30**, 185–187.
Islam, M. T., Rae, N. A., Glover, J. L., Barnea, Z., de Jonge, M. D., Tran, C. Q., Wang, J. & Chantler, C. T. (2010). *Phys. Rev. A*, **81**, 0229031.
Joly, Y., Cabaret, D., Renevier, H. & Natoli, C. R. (1999). *Phys. Rev. Lett.* **82**, 2398–2401.
Jonge, M. D. de, Barnea, Z., Tran, C. Q. & Chantler, C. T. (2004*a*). *Phys. Rev. A*, **69**, 022717.
Jonge, M. D. de, Barnea, Z., Tran, C. Q. & Chantler, C. T. (2004*b*). *Meas. Sci. Technol.* **15**, 1811–1822.
Jonge, M. D. de, Tran, C. Q., Chantler, C. T. & Barnea, Z. (2006). *Opt. Eng.* **45**, 046501.
Jonge, M. D. de, Tran, C. Q., Chantler, C. T., Barnea, Z., Dhal, B. B., Cookson, D. J., Lee, W. K. & Mashayekhi, A. (2005). *Phys. Rev. A*, **71**, 032702.
Jonge, M. D. de, Tran, C. Q., Chantler, C. T., Barnea, Z., Dhal, B. B., Paterson, D., Kanter, E. P., Southworth, S. H., Young, L., Beno, M. A., Linton, J. A. & Jennings, G. (2007). *Phys. Rev. A*, **75**, 032702.
Kas, J. J., Rehr, J. J., Glover, J. L. & Chantler, C. T. (2010). *Nucl. Instrum. Methods Phys. Res. A*, **619**, 28–32.
Kirsanov, M. A. & Obodskiy, I. M. (2010). *Instrum. Exp. Tech.* **53**, 185–193.
Laubert, S. (1941). *Ann. Phys. (Leipzig)*, **40**, 553–578.
Lytle, F. (2007). *Synchrotron Radiat. News*, **20**, 9–10.
McCrary, J. H., Plassmann, E. H., Puckett, J. M., Conner, A. L. & Zimmermann, G. W. (1967). *Phys. Rev.* **153**, 307–312.
Mica, J. F., Martin, L. J. & Barnea, Z. (1985). *J. Phys. C*, **18**, 5215–5223.
Nordfors, B. (1960). *Ark. Fys.* **18**, 37–47.
Park, S. H., Kim, H. S., Kim, Y. K., Kang, S. M., Kim, J. C. & Kim, J. K. (2005). *Radiat. Phys. Chem.* **73**, 248–253.
Parrish, E., Wilson, A. J. C. & Langford, J. I. (1999). *International Tables for Crystallography*, Vol. C, Section 5.2.10. Dordrecht: Kluwer Academic Publishers.
Pettifer, R. F., Borowski, M. & Loeffen, P. W. (1999). *J. Synchrotron Rad.* **6**, 217–219.
Rae, N. A., Chantler, C. T., Barnea, Z., de Jonge, M. D., Tran, C. Q. & Hester, J. R. (2010). *Phys. Rev. A*, **81**, 022904.
Rae, N. A., Chantler, C. T., Tran, C. Q. & Barnea, Z. (2006). *Radiat. Phys. Chem.* **75**, 2063–2066.
Rae, N. A., Islam, M. T., Chantler, C. T. & de Jonge, M. D. (2010). *Nucl. Instrum. Methods Phys. Res. A*, **619**, 147–149.
Rao, V. V. & Shahnawaz (1978). *Il Nuovo Cimento*, **A44**, 181–186.
Rehr, J. J. & Albers, R. C. (2000). *Rev. Mod. Phys.* **72**, 621–654.
Rehr, J. J. & Ankudinov, A. L. (2001). *J. Synchrotron Rad.* **8**, 61–65.
Saloman, E. B., Hubbell, J. H. & Scofield, J. H. (1988). *At. Data Nucl. Data Tables*, **38**, 1–196.
Smale, L. F., Rae, N. A., Chantler, C. T., Tran, C. Q. & Barnea, Z. (2006). *Radiat. Phys. Chem.* **75**, 1559–1563.
Takata, N., Yin, Z. & Li, A. (1999). *IEEE Trans. Nucl. Sci.* **46**, 326–332.
Tran, C. Q., Barnea, Z., de Jonge, M. D., Dhal, B. B., Paterson, D., Cookson, D. J. & Chantler, C. T. (2003). *X-ray Spectrom.* **32**, 69–74.
Tran, C. Q., Chantler, C. T. & Barnea, Z. (2003). *Phys. Rev. Lett.* **90**, 257401.
Tran, C. Q., Chantler, C. T., Barnea, Z. & de Jonge, M. D. (2004). *Rev. Sci. Instrum.* **75**, 2943–2949.
Tran, C. Q., Chantler, C. T., Barnea, Z., de Jonge, M. D., Dhal, B. B., Chung, C. T. Y., Paterson, D. & Wang, J. (2005). *J. Phys. B At. Mol. Opt. Phys.* **38**, 89–107.
Tran, C. Q., de Jonge, M. D., Barnea, Z. & Chantler, C. T. (2004). *J. Phys. B At. Mol. Opt. Phys.* **37**, 3163–3176.
Unonius, L. & Suortti, P. (1989). *J. Appl. Cryst.* **22**, 46–52.
Wang, D. C., Ding, X. L., Wang, X. F., Yang, H., Zhou, H. Y., Shen, X. Y. & Zhu, G. H. (1992). *Nucl. Instrum. Methods Phys. Res. B*, **71**, 241–248.
Wang, D. C., Yang, H. & Wang, X. M. (1994). *Nucl. Instrum. Methods Phys. Res. B*, **86**, 236–240.